Astronomy & Astrophysics manuscript no.
(DOI: will be inserted by hand later)

December 17, 2003

A new set of spectral indicators for type Ia supernovae

Correlations with absolute luminosity

G. Folatelli, G. Garavini, A. Goobar, S. Nobili,...

Department of Physics, Stockholm University,
SCFAB, SE-106 91 Stockholm, Sweden

Received ...; accepted ...

Abstract. We define a new set of empirical spectral quantities similar to equivalent widths (EW). These have been used to characterize the spectral homogeneity of type Ia supernovae (SNe Ia), their evolution with phase and to search for correlations with lightcurve properties and intrinsic brightness. A remarkable degree of homogeneity was found, including both 1991T- and 1991bg-like objects, in the cases of the features we name "Fe II 4800", "Mg II 4300" and "Ca II IR". Average evolutionary curves were built for Branch normal SNe to represent the general change of EW in time. The inhomogeneities among SNe Ia subtypes were found to stand out in the cases of the Si II features ("Si II 4000", "Si II 5800" and "Si II 6150"). At times around maximum light the EW of these features serve to distinguish clearly among SNe Ia subtypes. One of the studied spectroscopic indicators (measured at $\lambda \sim 4000$ Å) appears particularly promising as luminosity calibrator. The observed scatter in $M_B^{\max}$ was reduced to a value ≤ 0.14 mag for a sample of 10 nearby SNe with $0.70 < \Delta m_{15}(B) < 1.73$. This small scatter is probably dominated by the uncertainty in the distance estimates to those supernovae. Several other spectral indicators introduced are also measurable on optical spectra of high-z SNe, since they involve the blue part of the spectrum in the rest frame.

Key words.

1. Introduction

Type Ia supernovae (SNe Ia) have been successfully used as standardized candles for distance measurements and thus to probe the expansion history of the Universe. However, the physical nature of SNe Ia is not well understood. The most widely accepted model for SNe Ia involves a degenerate C+O white dwarf accreting material from a companion star (Whelan & Iben, 1973; Nomoto, 1982; Iben & Tutukov, 1984; Paczyński, 1985). The nature of the secondary component in the binary system as well as the explosion mechanism leading to a supernova event remain open questions (for review, see e.g. Hillebrandt & Niemeyer (2000)). Furthermore, systematic effects of evolutionary or environmental origin have been proposed as alternatives to the cosmological explanations of the faintness of the high-z SNe Ia. The study of lightcurve and spectral properties is a tool for understanding the physics of SNe Ia and for testing the accuracy of the standard candle hypothesis.

Classification and *qualitative* analysis of Type Ia spectra are a first and important step in the progress toward an understanding of SNe Ia (Filippenko, 1997). As high-quality data-sets of SNe begin to become available, we are now able to pursue more thorough, *quantitative* studies. Some pioneering work has been done in the search for correlations between spectral characteristics and lightcurve properties, attaining in some cases theoretical explanations associated with physical properties of the SNe or their environment. Nugent et al. (1995) note two spectral signatures which correlate with luminosity in a spectral sequence that they parametrize with the effective temperature of the SNe. They introduce the correlation with luminosity of the so-called silicon ratio [$\mathcal{R}$(Si II)] and calcium ratio [$\mathcal{R}$(Ca II)]. Another easy to measure spectral signature is the blueshift of certain absorption lines. In particular, Branch & van den Bergh (1993) define the parameter v_{10}(Si II) which denotes the velocity that corresponds to the blueshift of the minimum of the line normally attributed to Si II λ6355 measured 10 days after maximum light. This parameter was used to determine that there is a degree of spectroscopic heterogeneity among SNe Ia. More recently, Hatano et al. (2000) used the relationship between $\mathcal{R}$(Si II) and v_{10}(Si II) to claim that this heterogeneity is of multidimensional nature and might imply the coexistence of different explosion mechanisms for SNe Ia.

The present analysis is purely empirical and is motivated by the observation that different subtypes of SNe Ia

Send offprint requests to: Gastón Folatelli; gaston@physto.se

generally show absorption features of different strengths. From the point of view of spectroscopy, three subtypes can be distinguished (Branch et al., 1993). Spectroscopically normal SNe Ia, also referred to as *Branch normals*, are the ones whose optical spectra resembles those of SN 1981B (Branch et al., 1983), SN 1989B (Barbon et al., 1990), SN 1992A (Kirshner et al., 1993), and SN 1972E (Kirshner et al., 1973). Peculiar SNe Ia can be divided in two kinds, with SN 1991T (Filippenko et al., 1992a; Phillips et al., 1992; Ruiz-Lapuente et al., 1992; Jeffery et al., 1992; Mazzali et al., 1995) and SN 1991bg (Filippenko et al., 1992b; Leibundgut et al., 1993; Turatto et al., 1996; Mazzali et al., 1997) as prototypes. Before maximum light, 1991T-like SNe show unusually weak lines of intermediate-mass elements, yet some prominent lines due to Fe III. Their spectra at these early stages look featureless compared to those of normal SNe Ia. These differences become progressively less evident after maximum light. On the opposite extreme, 1991bg-like SNe show strong Ti II lines which produce a broad absorption trough from ~4100 to 4400 Å —lasting for several weeks after maximum— and enhanced absorption around 5800Å. Around maximum light, absorption lines for these SNe are generally stronger than those of normal SNe Ia. Based on the lightcurve width parameters —$\Delta m_{15}(B)$ (Phillips, 1993; Phillips et al., 1999) or stretch (Perlmutter et al., 1997; Goldhaber et al., 2001)— and their relation to luminosity, 1991bg-like SNe are also referred to as *under-luminous* or *fast-decliners*, and 1991T-like SNe as *slow-decliners*. There is exceptions to this classification and to the analogy between lightcurve and spectral properties. Objects discovered more recently present a higher degree of peculiarities, e.g. SN 2000cx (Li et al., 2001), and SN 2002cx (Li et al., 2003).

Based on a large spectroscopic data-set of SNe Ia, including several peculiar objects, this work presents a novel set of measurements which are analogous to equivalent widths (EW). We carry out the analysis of these measurements with a threefold goal:

(a) Provide empirically derived quantities of SN Ia spectra as a function of epoch.
(b) Quantify the spectral homogeneity of SNe Ia.
(c) Look for spectral calibrators to sharpen the standard candle nature of SNe Ia.

Section 2 briefly describes the two sets of spectroscopic data used in this work. Section 3 introduces the definitions on which the measurements in this work are based and the way systematic errors were controlled and final uncertainties estimated. The analysis of results is divided between Sec. 4 and Sec. 5. The former presents the measurements and time evolution for each spectral feature considered. The latter introduces some applications of spectral measurements to the use of SNe Ia as distance estimators in cosmology. Finally, Sec. 6 summarizes this work and comments on future prospects.

2. Data Description

This work uses two sets of spectroscopic data: **Set A** - 77 spectra from 13 SNe Ia discovered and followed by the Supernova Cosmology Project (SCP) in collaboration with members of the EROS (Hardin et al., 2000), the QUEST (Schaefer et al., 1999), and the Nearby Galaxies SN Search (Gal-Yam et al., 1999) teams. More details about these data can be found in Table 1; **Set B** - 89 published spectra from 8 well-observed, nearby objects. See Table 2 for a summary on these data.

Data from **Set A** were reduced and processed according to the method described in Folatelli et al. (2003). They consist of flux-calibrated spectra which were additionally corrected for atmospheric and Galactic extinction (Cardelli et al., 1989; Schlegel et al., 1998). Measured broad-band colors were used to "tilt" the spectra when discrepancies greater than the estimated calibration uncertainties (typically in the range of 5 to 10% of the total flux) were found. The spectra were put in the SN rest-frame using the redshifts (z) given in Table 1.

All the spectra in **Set A** include estimated statistical uncertainties for each wavelength bin. This was possible thanks to the use of the reduction method described in Folatelli et al. (2003), which keeps track of the measurement uncertainties through all reduction steps. A subset of these spectra showed some degree of host-galaxy light contamination, especially at late times. This contribution was estimated and subtracted in cases where it exceeded 10% of the total flux.

The spectra from **Set B** were taken from a number of sources (see Table 2). The flux calibrated spectra were put to rest-frame using the redshifts in Table 2. Finally, the spectra were tested and corrected when needed by use of available broad-band photometry. Given the absence of published uncertainties on these spectra, mean Poisson errors were estimated from point-to-point dispersion.

These two sets include some peculiar SNe Ia, including the prototypes of the two subclasses: SN 1991T and SN 1991bg. SN 1999aa (Garavini et al., 2003), SN 1999aw (Strolger et al., 2002), and SN 1999bp (first analyzed in this work) are included in the 1991T-like subclass. All these SNe present values of the lightcurve-shape parameter $\Delta m_{15}(B) < 1.0$ and are thus slow decliners. On the other extreme, SN 1986G (Phillips et al., 1987; Cristiani et al., 1992) and SN 1999by (Vinkó et al., 2001; Garnavich et al., 2001) belong to the 1991bg-like subclass. These are fast decliner SNe, with $\Delta m_{15}(B) > 1.70$. The case of SN 1999ac is considered separately. This SN presents photometric and spectroscopic peculiarities which make it a unique object: its lightcurve shows a slow rise similar to SN 1991T but a fast decline (Phillips et al., 2002) and its spectrum is similar to SN 1999aa (Garavini et al., 2003).

Table 1. SNe from **Set A** (SCP data).

SN	z	Host Galaxy	Galaxy Type[a]	Observed Epochs[b]
1999aa	0.0144	NGC 2595	SAB(rs)c	−11, −3, −1, 5, 6, 14, 19, 25, 28, 33, 40, 47, 51, 58
1999ac	0.0095	NGC 6063	Scd	−15, −9, 0, 2, 8, 11, 16, 24, 28, 31, 33, 39, 42
1999ao	0.054	Anon.	S:	5, 7, 10, 13, 18, 34, 40
1999au	0.124	Anon.	S:	12, 17
1999av	0.05	Anon.	E/S0:	2, 5, 9, 31
1999aw	0.038	Anon.	(?)	3, 5, 9, 12, 16, 24, 31, 38
1999be	0.019	Anon.	(?)	14, 19, 26, 33, 37, 44
1999bk	0.096	Anon.	E/S0:	4, 7, 9
1999bm	0.143	Anon.	S:	3, 6, 21
1999bn	0.129	Anon.	S:	2, 14, 22
1999bp	0.077	Anon.	S:	−2, 0, 1, 6, 17, 23
1999bq	0.149	Anon.	E/S0:	3, 18
1999by	0.0021	NGC 2841	SA(r)b	1, 6, 16, 27, 34

[a] Hubble type of the host galaxy. An entry followed by a colon is a classification based on the host galaxy spectrum. The rest is taken from the NED[1]

[b] Rest-frame days since B-band maximum light.

Table 2. SNe from **Set B** (Public data).

SN	z ($\times 10^{-3}$)	Host Galaxy	Galaxy Type[a]	Epochs[b]	Sources
1981B	6.031	NGC 4536	SAB(rs)bc	0, 17, 26, 29, 35, 49	1
1986G	1.825	NGC 5128	SO pec	−7, −5, −1, 0 ,3, 21, 28, 41, 44, 55	2
1989B	2.425	NGC 3627	SAB(s)b	−7, −5, −3, −2, −1, 3, 5, 8, 9, 11, 16, 18, 19	3
1990N	3.369	NGC 4639	SAB(rs)bc	−14, −7, 7, 14, 17, 38	4, 5, 6
1991bg	3.536	NGC 4374	E1	−2, 0, 13, 16, 23, 24, 30, 31, 44, 52	7, 8
1991T	5.791	NGC 4527	SAB(s)bc	−11, −9, −8, −7, −6, −5, −3, 0, 10, 15, 23, 24, 42, 45	9, 10, 11, 12
1992A	6.261	NGC 1380	SA0	−5, −1, 3, 7, 9, 11, 16, 17, 24, 28, 37, 46	13
1994D	1.49	NGC 4526	SAB(s)	−10,−9,−8,−7,−5,−3, 2, 4, 6, 8, 11, 13, 14, 16, 18, 20, 25	14, 15

[a] Hubble type of the host galaxy from the NED[1].

[b] Rest-frame days since B-band maximum light.

Sources: (1) Branch et al. (1983); (2) Phillips et al. (1987); (3) Wells et al. (1994); (4) Leibundgut et al. (1991); (5) Phillips et al. (1992); (6) Mazzali et al. (1993); (7) Filippenko et al. (1992b); (8) Leibundgut et al. (1993); (9) Filippenko et al. (1992a); (10) Ruiz-Lapuente et al. (1992); (11) Phillips et al. (1992); (12) Jeffery et al. (1992); (13) Kirshner et al. (1993); (14) Meikle et al. (1996); (15) Patat et al. (1996).

3. Spectral Indicators

3.1. Feature Definitions

Centered on the location of the strongest absorption features in near-maximum SN Ia spectra, eight regions bounded by local spectral flux maxima have been defined. Figure 1 shows these regions as they are defined at different epochs. Each feature is marked with a number from 1 to 8 and each number corresponds to a label name. These names are related to an ion or a line responsible for at least part of the observed feature at some epoch.

The ranges over which the upper and lower limits of features are defined are given in Table 3. These limits vary in time, and from SN to SN, following the spectral evolution. The choice of the limits in each case depends on the definition of the measurement itself and will be described in detail in the next paragraph.

3.2. Equivalent Widths

The measurements introduced in this paper are of the nature of equivalent widths (EW). However, in order to measure an EW, the continuum must be determined and this is not well defined in SNe Ia spectra, particularly after maximum light. For simplicity, we define a pseudo-continuum as the straight line fit through the two local maxima that bound a feature (see panel **(b)** in Fig. 1). The inability to

[1] The NASA/IPAC Extragalactic Database (NED) is operated by the Jet Propulsion Laboratory, California Institute of Technology, under contract with the National Aeronautics and Space Administration.

Table 3. Feature limits.

ID	Feature Label	Blue-ward limit range (Å)	Red-ward limit range (Å)
1	"Ca II H&K"	3500 – 3800	3900 – 4100
2	"Si II 4000"	3900 – 4000	4000 – 4150
3	"Mg II 4300"	3900 – 4150	4450 – 4700
4	"Fe II 4800"	4500 – 4700	5050 – 5550
5	"S II W"	5150 – 5300	5500 – 5700
6	"Si II 5800"	5550 – 5700	5800 – 6000
7	"Si II 6150"	5800 – 6000	6200 – 6600
8	"Ca II IR"	7500 – 8000	8200 – 8900

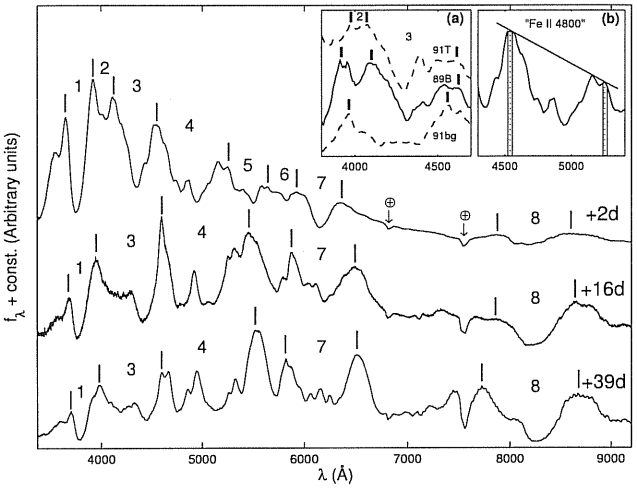

Fig. 1. SNe Ia spectral evolution and feature definitions for three epochs: 2, 16 and 39 days after maximum light. Numerical labels correspond to the following adopted feature names: **1**- "Ca II H&K"; **2**- "Si II 4000"; **3**- "Mg II 4300"; **4**- "Fe II 4800"; **5**- "S II W"; **6**- "Si II 5800"; **7**- "Si II 6150"; and **8**- "Ca II IR". Short vertical lines show the approximate positions where the pseudo-continuum is taken in each case. Feature ranges change with time and, due to blending, some weaker features are not considered at later epochs. Note that, as the SNe leave the photospheric phase, pseudo-continuum points correspond to emission peaks. *Panel* (**a**): the region of features #2 and #3 for near-maximum spectra of SN 1991T (top), SN 1989B (middle), and SN 1991bg (bottom). Feature #2 is not defined in the case of 1991bg-like SNe. Adopted feature limits are marked with vertical lines. *Panel* (**b**): an example of the pseudo-continuum trace for "Fe II 4800" on a normal SN Ia near the time of maximum light. Here, solid vertical lines show the regions where the pseudo-continuum is fitted. Dotted lines mark the measurement limits.

determine the actual continuum level prevents us from deriving the physical interpretation assigned to EW of single, narrow lines of stars. Nevertheless, this does not prevent us from building well-defined quantities and thus a consistent set of measurements for all SNe.

Given the complexity of SNe Ia spectra, within the limits given in Table 3, at each side of a feature there may be several local maxima. The chosen maxima are the ones that maximize the wavelength span of the feature with the restriction that the derived pseudo-continuum does not cross the spectrum within the feature limits.

This criterion for the selection of the feature bounds is also applied to feature mergers. A merger occurs when a single straight-line pseudo-continuum trace can be applied to the whole region encompassing two features without cutting the spectrum. Consequently, the three weakest features, namely #2 ("Si II 4000"), #5 ("S II W"), and #6 ("Si II 5800"), are defined over a limited time around maximum light. Eventually, they become blended with neighboring, stronger features, whose label is then used. Feature #2 ("Si II 4000") merges #3 ("Mg II 4300"); feature #5 "S II W" merges #4 ("Fe II 4800"); and feature #6 "Si II 5800" merges #7 ("Si II 6150"). These mergers may occur at different epochs for different SNe.

Once the continuum is traced, the EW is computed for each feature within its wavelength limits. The spectrum is normalized by the continuum and the resulting area of the feature is measured (in units of Å). In this case, the calculation was approximated by a simple rectangular integration method:

$$\mathrm{EW} = \sum_{i=1}^{N} \left(1 - \frac{f_\lambda(\lambda_i)}{f_c(\lambda_i)}\right) \Delta\lambda_i, \qquad (1)$$

where λ_i ($i = 1, \ldots, N$) are the central wavelength values of bins of size $\Delta\lambda_i$ over the span of the feature; $f_\lambda(\lambda_i)$ is the measured flux in each bin i; $f_c(\lambda_i)$ is the fitted continuum flux evaluated at the same points. Deviating points due to bad pixels or narrow host-galaxy lines were rejected using a 3σ-clipping algorithm.

A 1σ statistical uncertainty was computed by error propagation from the estimated errors in the spectral flux and in the fitted continuum:

$$\sigma_{\mathrm{EW}} = \left[\sum_{i=1}^{N} \left(\frac{\sigma_{f_i}^2(\lambda_i)}{f_c^2(\lambda_i)} + \frac{f_\lambda^2(\lambda_i)}{f_c^4(\lambda_i)}\sigma_{c_i}^2(\lambda_i)\right)(\Delta\lambda_i)^2\right]^{1/2}. \qquad (2)$$

Here, σ_{f_i} are the estimated measurement uncertainties on spectral flux and σ_{c_i} are the uncertainties in the fitted continuum flux. In the calculation of σ_{EW}, it was assumed that values in different wavelength bins are independent from each other and that numerical uncertainties arising from the integration method itself are negligible.

By definition, the EW is distance-independent and thus provides a useful tool for comparing spectra from different objects. Section 4 is dedicated to this analysis.

3.3. Systematic Effects

Systematic errors in the determination of the continuum reference points were accounted for by performing the fits on sliding windows (typically a quarter of the region used for the continuum fit to each side) and computing the weighted root-mean square deviation (rms) of the encountered EW's. This source of error was added geometrically to the one given in Eqn. 2. This was the dominant source

of uncertainties when the signal-to-noise ratio per resolution element was above ~10.

It is known that EW's can be affected by poor resolution or low signal-to-noise ratio of the spectra (Gray, 1992). These effects were tested by artificially treating the data. Boxcar smoothing was used to decrease the resolution of the best-sampled spectra and reproduce the range of resolutions in the present data set. Due to the nature of the broad SN features, even the lowest resolution available (~10 Å/pixel) did not produce any significant change of the measured EW.

In the present spectra sample, pixel-to-pixel signal-to-noise ratios ranged from about 5 to several hundred. When Gaussian noise was added to the best-quality spectra, in order to reproduce that quality range, no significant bias was detected on the resulting EW values.

Additionally, the effect of reddening was also tested by artificially adding it to several spectra up to a value of $E_{B-V} = 0.32$ (corresponding to $A_V = 1$ mag, with $R_V = 3.1$) following the law given in Cardelli et al. (1989). This produced no significant change in the resulting values for EW. The nature of these EW measurements, given by the point-to-point ratio of observed to continuum fluxes in a limited wavelength range, makes them insensitive to reddening.

Further systematic effects could arise from host-galaxy light contamination or other background sources which might not be well subtracted. The effect of additional signal underlying the SN spectrum would be to lower the values of EW. The published spectra from **Set B** in the present sample correspond to very bright, nearby SNe, for which SN and host-galaxy spectra can be resolved. For more distant SNe, from **Set A**, we used only the spectra where no significant contamination was found or when this could be reliably subtracted. We have tested this effect on a typical near-maximum light spectrum. Template galaxy spectra of Hubble types E and Sc were added to the SN spectrum in order to simulate contamination levels ranging from 0 to 50% of the total integrated flux between 3500 and 9000Å. The EW's of all eight features were then measured on every spectrum. The decrease of EW with increasing contamination levels was found to be approximately linear. Table 4 summarizes these results by giving the relative decrease of EW per each 10% of contamination, in the cases of both galaxy types. Since the SN at the epoch under consideration is relatively fainter on the red part of the spectrum, the effect is greater for features lying on that end. For early type galaxies, because of the presence of the Balmer break around 4000Å, the effect on the EW of "Ca II H&K" is less than 10% even for 50% contamination.

Table 4. The effect of host-galaxy contamination on the EW's.

	Feature	Host Type	
ID	Label	E	Sc
1	"Ca II H&K"	0.019	0.080
2	"Si II 4000"	0.048	0.074
3	"Mg II 4300"	0.037	0.073
4	"Fe II 4800"	0.070	0.074
5	"S II W"	0.112	0.074
6	"Si II 5800"	0.128	0.066
7	"Si II 6150"	0.103	0.084
8	"Ca II IR"	0.155	0.114

4. Spectral Evolution

A first use of EW is the study of their change in time as a way to characterize spectral evolution. Though empirically defined, consistency in the measuring procedure allows for a comparative analysis of their evolution with time. As the SN evolves from its hot photospheric phase, through maximum light, and finally into the nebular phase, both continuum and line properties vary. The evolution of the physical conditions in the ejecta as well as the recession of the photosphere produce variations in the spectral characteristics which result in changing EW values.

The following analysis is divided by spectral features. The first three sections are dedicated to features which show the greatest homogeneity, even among 1991T- and 1991bg-like SNe: features #4 ("Fe II 4800"), #8 ("Ca II IR"), and #3 ("Mg II 4300"). "Fe II 4800" and "Mg II 4300" fall in a region of the spectrum where several ions of intermediate-mass and iron-peak elements contribute to form fairly complex profiles. "Ca II IR", on the contrary, is believed to be due to the Ca II infrared triplet at all epochs, with little contamination from other ions. Subsequent sections involve features with more heterogeneous behavior, i.e. the three "Si II" features, "Ca II H&K" and "S II W". These features are believed to be formed by intermediate-mass elements around maximum light and eventually become contaminated by iron-peak element lines.

The epochs used in this analysis are based on lightcurve estimates. In the case of our **Set A**, preliminary lightcurves were used for determining the date of maximum B-band brightness and epochs were corroborated to within a few days by spectral shape comparison with precisely dated SNe. Given the uncertainties in dating, epochs were taken as the integer number of days since maximum light.

4.1. "Fe II 4800" (#4)

This feature shows a very smooth evolution in EW (see Fig. 2). In this evolution, there is a high degree of homogeneity for all the SNe in our sample. In general, the EW values increase from around 100Å before maximum light to 350Å three weeks after, with some hint of a decline from then on. The overall increase in the EW is mainly due to the rise of the emission peaks relative to the troughs between them. At epochs later than 15 days, this feature has become broader as a consequence of the blending of lines lying to the red (see Fig. 1). The exact epoch when this blending takes place depends on the SN. In general, it is

found to happen at later epochs for slow decliners and at earlier epochs for fast decliner SNe.

A mean evolutionary curve for the Branch normal SNe in our sample can be represented by a cubic spline function. The solid line in Fig. 2 shows this average curve. The curve was built in the range $-10\text{d} < \text{epoch} < 50\text{d}$ by dividing the epochs into 5 bins, calculating a weighted average of the EW in each bin, and finally tracing the spline function through those points. Individual objects evolve approximately parallel to the mean curve. In general, 1991bg-like SNe lie above the curve and 1991T-like SNe lie below it.

This is summarized in Table 5 which shows the distribution of the three SNe Ia subtypes with respect to the average curve. Column 1 lists the epoch bins in consideration. Column 2 gives the number of points from Branch normal SNe in each bin. Column 3 lists the average EW for normal SNe and its 1-σ uncertainty. Column 4 shows the r.m.s. dispersion of Branch normal SNe with respect to the average curve, which we name "δ". Columns 5 and 6 refer to 1991T-like SNe and show the number of points and the mean deviation from the average curve. Columns 7 and 8 show the same two quantities for the case of 1991bg-like SNe. The values in columns 6 and 8 are to be compared with δ. It can be seen that 1991T-like SNe show systematically negative deviations up to around a month after maximum light. The deviations are positive in the case of 1991bg-like SNe, although they are generally less significant —also, there are fewer data for this subtype.

4.2. "Ca II IR" (#8)

This broad feature located around 8000Å and usually assigned to a Ca II triplet with very little contamination from other elements, shows an evolutionary pattern which is similar to that of "Fe II 4800" (see Fig. 3). Fewer spectra in the present sample cover the region spanned by this broad feature, which reduces the statistical significance of these results. Fringing residuals and low sensitivity from some detectors can introduce higher noise and systematic uncertainties by affecting the trace of the pseudo-continuum. These effects were checked and the problematic spectra were excluded from the analysis.

Similarly to "Fe II 4800", the EW's start growing at maximum light and stabilize after approximately day +25, though the amplitude of the increase is greater in this case. Individual objects evolve in a nearly parallel manner, with the exception of the 1991bg-like SNe which show a slightly slower increase. The solid line in Fig. 3 represents a cubic spline function built with the data from normal SNe in 4 epoch bins between days −10 and +40. In general, 1991bg-like SNe lie above the average curve while 1991T-like SNe lie below it.

The deviations from the average curve are summarized in Table 6. The columns of this table are equivalent to those of Table 5. The distinction among the three families of SNe Ia is enhanced in the present case, although more data would be necessary to corroborate this in the case of 1991bg-like objects.

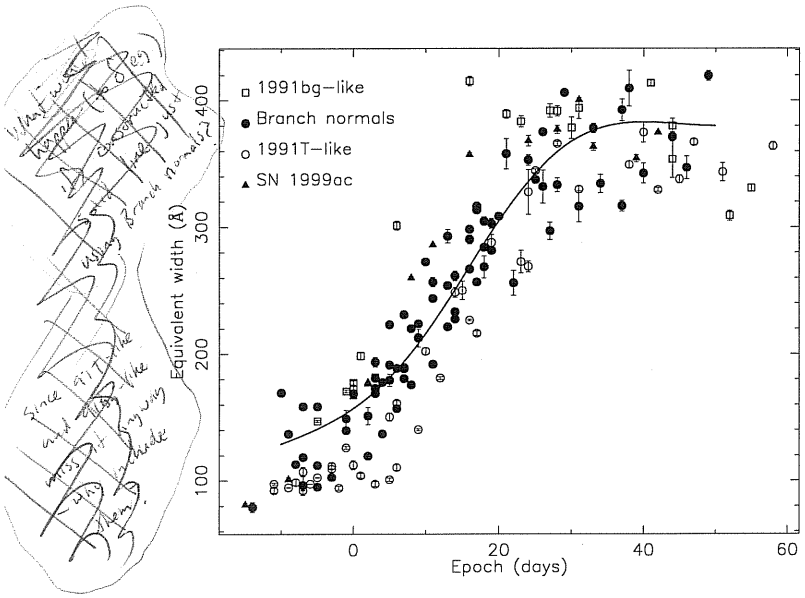

Fig. 2. Measured EW values corresponding to "Fe II 4800" (#4). Fast decliner SNe are marked with open squares, slow decliner SNe with open circles, normal SNe with filled circles and SN 1999ac with triangles. Error-bars are given by Eqn. 2 plus systematic uncertainties arising in the continuum fit. The solid line shows a cubic spline function used to represent the average evolution of normal SNe Ia in the sample, between days −10 and +50. In general, 1991bg-like SNe Ia lie above the average curve whereas slow decliner SNe Ia lie below it.

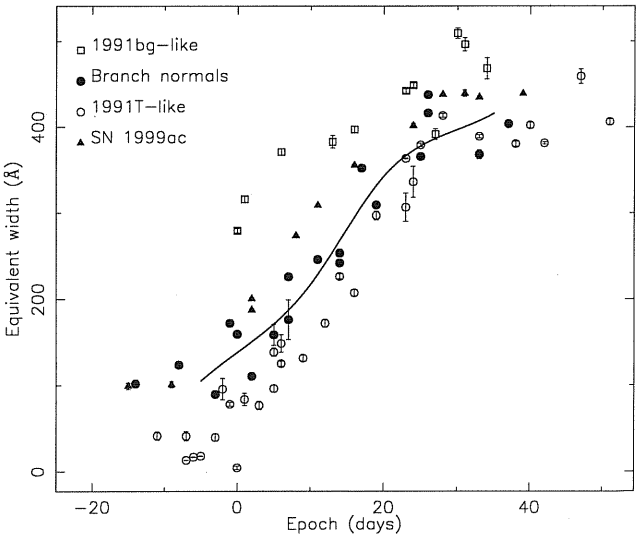

Fig. 3. Measured EW values corresponding to "Ca II IR" (#8). Fast decliner SNe are marked with open squares, slow decliner SNe with open circles, normal SNe with filled circles and SN 1999ac with triangles. Error-bars are given by Eqn. 2 plus systematic uncertainties arising in the continuum fit. The solid line shows a cubic spline function used to represent the mean evolution of normal SNe Ia. In general, 1991bg-like SNe Ia lie above the average curve whereas slow decliner SNe Ia lie below it.

Table 5. Dispersion of "Fe II 4800" EW for the three SNe Ia subtypes.

Epoch bin	Branch Normal n	$\langle$EW$\rangle$ (Å)	δ (Å)	1991T-like n	Δ_{EW} (Å)	1991bg-like n	Δ_{EW} (Å)
(1)	(2)	(3)	(4)	(5)	(6)	(7)	(8)
$[-10,-6]$	6	132 ± 11	28	5	-29 ± 3	0	...
$[-5,-1]$	6	114 ± 12	37	5	-36 ± 5	2	16 ± 4
$[0,5]$	12	164 ± 10	28	5	-62 ± 9	4	24 ± 7
$[6,11]$	15	200 ± 8	25	4	-58 ± 15	1	113 —
$[12,18]$	15	265 ± 9	25	5	-47 ± 12	1	139 —
$[19,27]$	10	316 ± 12	30	5	-34 ± 18	3	58 ± 8
$[28,40]$	9	353 ± 13	36	5	3 ± 9	3	37 ± 5

Columns: (1) Range of epoch bins in days; (2) Number of points for Branch normal SNe; (3) Average EW for Branch normal SNe; (4) Dispersion (rms) of normal SNe around the average curve; (5) Number of points for 1991T-like SNe; (6) Mean deviation of 1991T-like SNe from average curve; (7) Number of points for 1991bg-like SNe; (8) Mean deviation of 1991bg-like SNe from average curve.

Table 6. Dispersion of "Ca II IR" EW for the three SNe Ia subtypes.

Epoch bin	Branch Normal n	$\langle$EW$\rangle$ (Å)	δ (Å)	1991T-like n	Δ_{EW} (Å)	1991bg-like n	Δ_{EW} (Å)
(1)	(2)	(3)	(4)	(5)	(6)	(7)	(8)
$[-5,4]$	4	116 ± 21	40	7	-88 ± 25	2	155 ± 15
$[5,13]$	4	229 ± 19	39	6	-61 ± 8	2	161 ± 32
$[14,23]$	4	277 ± 25	31	5	-53 ± 18	2	90 ± 13
$[24,35]$	4	392 ± 17	43	4	-1 ± 12	5	63 ± 21

See column explanations in Table 5.

4.3. "Mg II 4300" (#3)

This feature is formed at different epochs by the overlap of lines from various ions. These include Mg II, Co II, Fe II, Fe III, and Si III for spectroscopically normal and 1991T-like SNe. In the case of 1991bg-like SNe, the region is dominated by strong lines of Ti II (Filippenko et al., 1992b; Mazzali et al., 1997). The EW evolution of this feature is not as smooth as in the two previous cases. As can be seen in Fig. 4, a more or less discontinuous evolutionary behavior is found here. This is related to blending with "Si II 4000" in coincidence with absorption deepening which makes the values of EW suddenly increase from ~100Å to ~250Å on time scales of less than a week. The phase at which this break takes place is highly dependent on the kind of object: for 1991bg-like SNe Ia it seems to occur as early as 5 days before maximum light (the earliest spectrum of a 1991bg-like SN in our sample), while normal SNe Ia show this behavior around one week after maximum light, and 1991T-like objects show it later than day +10.

The average evolution can be described by a function:

$$f(\boldsymbol{\theta}, t) = \frac{A}{e^{\frac{t_{br}-t}{\tau}} + 1} + B, \qquad (3)$$

with parameters $\boldsymbol{\theta} = (A, B, t_{br}, \tau)$. This type of function is useful to reproduce the step-like behavior observed and to parametrize the time when the break occurs (through t_{br}), which will be used in Sec. 5. The parameters were fitted to the data corresponding to normal SNe. The solid line in Fig. 4 shows this average curve between days −10 and +30. Nearly parallel evolutionary paths are followed by individual SNe varying systematically among SN families as in the cases of the two previously analyzed features. Table 7 lists the dispersion of normal SNe around the average curve and the deviations of 1991T-like and 1991bg-like SNe from the same curve. The largest deviations for 1991T-like SNe are found between one and two weeks after maximum light, due to the aforementioned lag in the occurrence of the break for these objects. The remarkable difference in EW seen between 1991bg-like SNe and the rest at times around maximum light is also found in the table.

4.4. "Si II" Features

This section describes the properties of three features which are assigned to Si II in near-maximum spectra and which are peculiar to SNe Ia: "Si II 4000", "Si II 5800" and "Si II 6150". Figures 5, 6 and 7 respectively show their EW evolution. These features are relatively weaker and more subject to contamination than the others treated in this work. "Si II 4000" blends into "Mg II 4300" a few days after maximum and is thereafter considered as part of it. "Si II 4000" is not considered in 1991bg-like SNe because

Table 7. Dispersion of "Mg II 4300" EW for the three SNe Ia subtypes.

Epoch	Branch Normal			1991T-like		1991bg-like	
bin	n	$\langle$EW$\rangle$ (Å)	δ (Å)	n	Δ_{EW} (Å)	n	Δ_{EW} (Å)
(1)	(2)	(3)	(4)	(5)	(6)	(7)	(8)
$[-10,-5]$	6	90 ± 7	16	6	15 ± 4	0	···
$[-4,0]$	6	98 ± 5	14	5	-5 ± 3	4	139 ± 22
$[1,5]$	9	118 ± 12	28	4	-25 ± 12	1	206
$[6,10]$	10	184 ± 14	26	4	-77 ± 12	0	···
$[11,17]$	15	251 ± 10	33	5	-69 ± 23	2	48 ± 2
$[18,30]$	15	257 ± 7	27	6	8 ± 6	4	21 ± 20

See column explanations in Table 5.

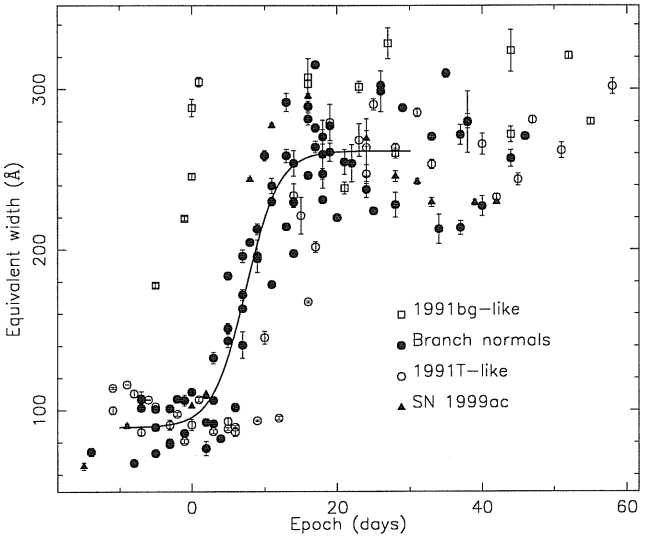

Fig. 4. Measured EW values corresponding to "Mg II 4300" (#3). Fast decliner SNe are marked with open squares, slow decliner SNe with open circles, normal SNe with filled circles and SN 1999ac with triangles. Error-bars are given by Eqn. 2 plus systematic uncertainties arising in the continuum fit. The solid line represents the average behavior of normal SNe Ia, fitted using the function of Eqn. 3. In general, 1991bg-like SNe Ia lie above the average curve whereas slow decliner SNe Ia lie below it.

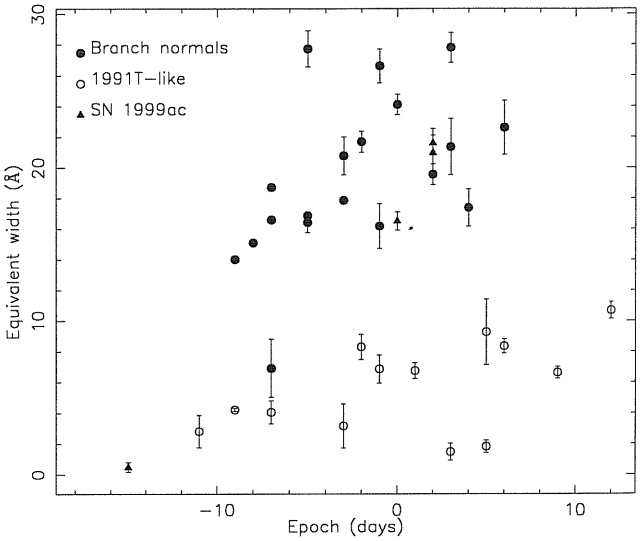

Fig. 5. Measured EW values corresponding to "Si II 4000" (#2). Slow decliner SNe with open circles, normal SNe with filled circles and SN 1999ac with triangles. Error-bars are given by Eqn. 2 plus systematic uncertainties arising in the continuum fit. Normal and 1991T-like SNe are clearly separated in two families.

of the presence of strong Ti II which blends it into a broad "Mg II 4300" feature. "Si II 5800" is considered until about 10 days after maximum light, when it becomes contaminated by the Na I D line (Branch et al., 1983). "Si II 6150" remains defined as such for later epochs, though Fe II lines on each side of it appear around 10 days past maximum and the feature becomes broader and structured.

The dispersion in EW is greater for the Si II features, as they show a clearer distinction among different kinds of SNe Ia. Single objects show increasing EW evolution, as is seen in other features, though in these cases no clear common behavior can be established for the whole set of SNe.

The EW of "Si II 4000" between days −10 and +10 for normal and 1991T-like SNe show a clear division into two families: (a) A group of SNe with very weak absorptions (EW < 10Å), including the 1991T-like objects and SN 1990N. (b) A group of normal SNe Ia plus SN 1999ac, with EW > 15Å. On average, there is a factor of 4 difference in EW between the two groups.

"Si II 5800" is very strong in 1991bg-like SNe, for which the main contribution was first attributed to the Na I D line (Filippenko et al., 1992b) and more recently to Ti II (Garnavich et al., 2001). These SNe clearly separate from the rest, with values of EW ≈ 50Å. The distinction between normal and 1991T-like SNe is also found here, as in the case of "Si II 4000".

Less dispersion is found in the case of "Si II 6150". EW's scatter the most before maximum light, differing on a factor of 2 between extremes. Fast decliner SNe show absorption strengths similar to those of normal SNe up to 20 days past-maximum light. Afterward, they seem to stabilize whereas normal SNe keep increasing. SN 1991T-

I think we might consider restating this if we plot Fig 5 and Fig 6 on the same scale (axes) as Fig 3. Then they look very similar to (a small time window of) previous plots.

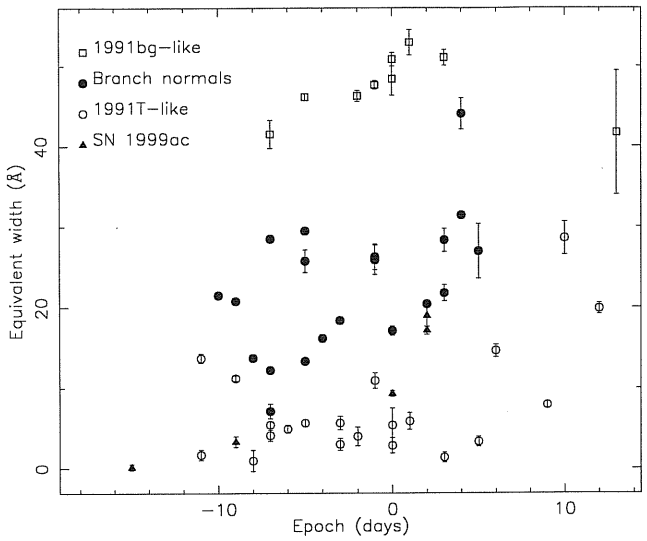

Fig. 6. Measured EW values corresponding to "Si II 5800" (#6). Fast decliner SNe are marked with open squares, slow decliner SNe with open circles, normal SNe with filled circles and SN 1999ac with triangles. Error-bars are given by Eqn. 2 plus systematic uncertainties arising in the continuum fit. This diagram clearly separates the three SN Ia subtypes.

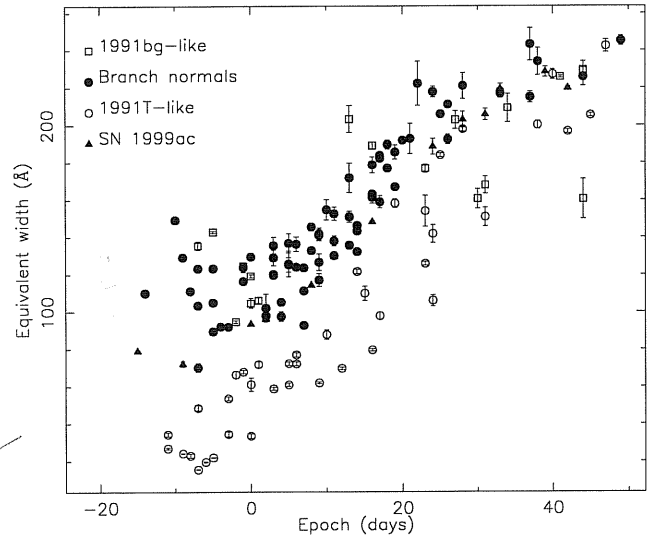

Fig. 7. Measured EW values corresponding to "Si II 6150" (#7). Fast decliner SNe are marked with open squares, slow decliner SNe with open circles, normal SNe with filled circles and SN 1999ac with triangles. Error-bars are given by Eqn. 2 plus systematic uncertainties arising in the continuum fit. The distinction between 1991T-like objects and the rest is evident around maximum light up to day +25.

like objects show significantly weaker "Si II 6150" before and around maximum light and become closer to normal SNe at times later than about two weeks. SN 1999ac marks a division between 1991T-like SNe and the rest throughout the epochs analyzed.

The Si II features are important in classifying SNe Ia as such and, furthermore, in distinguishing between subclasses. The present measurements serve in quantifying the differences among those subclasses. The pair "Si II 6150" - "Si II 5800" can be easily identified in optical spectra of low redshift SNe. However, at higher redshift ($z > 0.5$) optical spectra only cover "Si II 4000" among the three. Therefore, the analysis of this feature becomes crucial when applied to high-redshift SN samples.

4.5. "Ca II H&K"

The prominent absorption trough found around 3800Å is attributed mainly to the H and K lines of Ca II with some contribution from Si II λ3858. Fig. 8 shows the measurements on this feature. In the case of SN 1991T, this feature is particularly weak. This could be due to lower abundances of Ca II or to a temperature effect. Fisher et al. (1999) marginally attributes this feature to Ni II on the early spectra of SN 1991T.

This feature breaks the trend relating absorption strengths and lightcurve shapes, as was found for the previously analyzed features. The SNe Ia subtypes are not distinguished or in any order of EW. An additional peculiarity is that in general the EW do not increase with phase. The evolutionary behavior is dependent on the object both qualitatively and quantitatively. The dispersion on EW is greater before maximum light, where some objects show an increase and others a decrease. After maximum light, there is normally a slow decrease, except for the 1991bg-like objects which maintain or increase their EW.

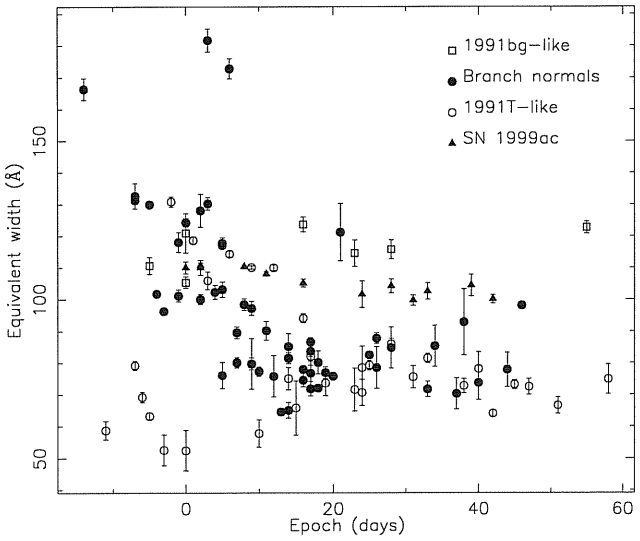

Fig. 8. Measured EW values corresponding to "Ca II H&K" (#1). Fast decliner SNe are marked with open squares, slow decliner SNe with open circles, normal SNe with filled circles and SN 1999ac with triangles. Error-bars are given by Eqn. 2 plus systematic uncertainties arising in the continuum fit.

The two points with EW > 170Å after day 0 belong to SN 1999bm. Their large EW values are due to an unusually

broad "Ca II H&K" feature. This phenomenon might be caused by the presence of a strong, high-velocity Ca II component, as suggested in the case of the Ca II IR triplet for SN 2001el (Wang et al., 2003). The signal-to-noise ratio of the spectra of SN 1999bm in the region around 8000 Åto determine the presence of such a component.

4.6. "S II W"

The analysis of this feature is limited to the time range when it shows its distinct "W"-like shape, i.e. up to 7 days after maximum light. Its EW values are plotted in Fig. 9. Though the dispersion around maximum is large, the distinctions seen in previously discussed features are not present here. Fast decliner, normal and 1991T-like SNe seem not to be distinguishable through the EW corresponding to this feature.

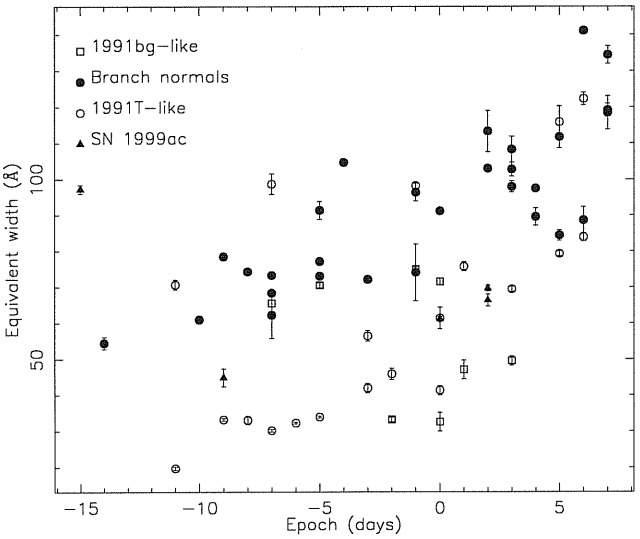

Fig. 9. Measured EW values corresponding to "S II W" (#5). Fast decliner SNe are marked with open squares, slow decliner SNe with open circles, normal SNe with filled circles and SN 1999ac with triangles. Error-bars are given by Eqn. 2 plus systematic uncertainties arising in the continuum fit. A large dispersion among all the SNe is found and no clear distinction of the different subtypes.

5. EW and the Standard Candle Calibration

The use of SNe Ia for measuring precise cosmological distances is based on the refinement of the standard candle through calibration of its luminosity at maximum light (e.g. the peak absolute B-band magnitude, $M_B^{\max}$). The calibration of $M_B^{\max}$ is usually done through its correlation with a lightcurve shape parameter like $\Delta m_{15}(B)$, or stretch (s). In this work we attempt to use spectroscopic indicators to achieve similar and complementary results. In the following, a number of correlations between EW measurements and $M_B^{\max}$ or $\Delta m_{15}(B)$ are presented. Other spectral parameters were tested for correlations to $M_B^{\max}$ with no conclusive results and are thus not included in this analysis.

As a reference for the next sections, Table 8 summarizes the relevant data used and the correlations found for the sample of SNe Ia studied in this section. Columns 2 and 3 respectively give the values of $M_B^{\max}$ and $\Delta m_{15}(B)$. The latter were found by fitting the template B-band lightcurve given by Goldhaber et al. (2001) to the photometry data. Column 4 shows the residual magnitudes from the parabolic relation between $M_B^{\max}$ and $\Delta m_{15}(B)$ given by Phillips et al. (1999). The data in column 2 were used to fit the intercept of such a relation —the value of $M_B^{\max}$ at $\Delta m_{15}(B) = 1.1$, which was found to be -19.18 ± 0.08. The relation, originally given for the range $0.85 \leq \Delta m_{15}(B) \leq 1.70$, was extended to the extreme values of $\Delta m_{15}(B)$ of the present SN sample.

The values of $M_B^{\max}$ are based on observed peak B-band magnitudes, extinction estimates and distances to the host galaxies. The distance moduli, the estimation methods used and the corresponding references are listed in columns 5 through 7. Column 8 gives the total color excess (E_{B-V}) due to reddening in the Galaxy and in the host galaxy. The values for SN 1999aa, SN 1999ac, and SN 1999bp correspond to reddening in the Galaxy only. Column 9 shows the references for host galaxy reddening estimates. The Galactic reddening was taken from Schlegel et al. (1998).

For very nearby SNe, published distance estimates were used. It should be noted that the different methods, and even different authors using the same method, can yield systematically inconsistent results. For example, systematic differences of ∼0.2–0.3 mag (∼10% in distance) are found between the results of the two teams which use cepheids observed with the *Hubble Space Telescope* (Saha et al., 1996, 1997, 1999; Freedman et al., 2001). Both teams measured a distance to the hosts of SN 1981B, SN 1989B, and SN 1990N, showing those discrepancies. We decided to use the results from Freedman et al. (2001). For SN 1991T, there are distance estimates by Saha et al. (2001) and Gibson & Stetson (2001). We chose to use the latter because their estimate of the Hubble constant is in agreement with the one by Freedman et al. (2001). In general, for these nearby objects, the uncertainties in the distance and in the extinction are the ones that dominate the errors on $M_B^{\max}$. All of this must be borne in mind when considering the correlations presented below.

For more distant SNe, with no available measurement of the distance to the host galaxy, the value of recession velocities and a standard value of the Hubble constant ($H_\circ = 72 \pm 3$ km s^{-1} Mpc^{-1}, from Freedman et al. (2001)) were used. Uncertainties in the recession velocities due to peculiar motion were considered to be 300 km s^{-1}. The uncertainties in $H_\circ$ dominate. Among these SNe, a value of extragalactic extinction was available only for SN 1999aw (Strolger et al., 2002). Since these objects are fainter, the uncertainties on their $M_B^{\max}$ show comparable contribu-

Table 8. Lightcurve parameters and spectral indicators for some SNe Ia.

SN	$M_B^{\max}$ [a]	$\Delta m_{15}(B)$[a]	ΔM_B[a]	Distance Modulus[a]	Distance Method	Ref.[j]	E_{B-V}[a] (Total)	Ref.[k]	$\mathcal{R}(\text{Si II})_{\text{EW}}$[b]	$\mathcal{R}(\text{Si II})$[c]	t_{br}[d] (d)	$\text{EW}^{\max}_{(2+3)}$ (Å)	$\alpha_{(2+3)}$ (Å d^{-1})
(1)	(2)	(3)	(4)	(5)	(6)	(7)	(8)	(9)	(10)	(11)	(12)	(13)	(14)
1981B	−19.23(25)	1.22(09)	−0.19	30.87(15)	Cepheids	1	0.13(03)	1	0.16(05)	0.132(008)	···	25.3 ± 1.3[h]	···
1986G	−17.72(42)	1.73(05)	0.48	27.71(08)	SBF	2	0.61(05)	1	0.53(05)	0.413(008)	1.7	130.5 ± 5.5	13.2 ± 1.9
1989B	−19.15(20)	1.32(07)	−0.21	30.01(15)	Cepheids	1	0.37(04)	1	0.29(05)	0.179(011)	7.1	22.2 ± 1.2	2.5 ± 0.3
1990N	−19.01(16)	1.03(10)	0.19	31.71(15)	Cepheids	1	0.12(03)	1	0.16(05)	0.205(004)	9.2	17.0 ± 7.4	1.9 ± 0.7
1991T	−19.56(23)	0.96(07)	−0.32	30.56(09)	Cepheids	3	0.16(05)	1	0.14(05)	0.032(031)	12.1	-22.9 ± 3.0	-3.0 ± 0.5
1991bg	−16.54(32)	1.93(05)	1.52[e]	31.09(30)	SBF	4	0.05(02)	2	0.62(05)	0.474(014)	< 0[g]	178.3 ± 5.4[h]	···
1992A	−18.79(16)	1.45(04)	0.00	31.35(16)	G.Clusters	5	0.02(02)	1	0.38(05)	0.235(008)	7.0	13.3 ± 1.7	5.3 ± 0.6
1994D	−18.67(30)	1.46(10)	0.11	30.40(30)	G.Clusters	6	0.06(03)	3	0.29(05)	0.211(002)	7.0	-4.1 ± 1.4	3.2 ± 0.4
1999aa	−19.14(78)	0.95(08)	0.25	33.89(77)	$d = cz/H_o$[f]	7	(0.040)	···	0.25(03)	0.163(016)	13.6	-19.4 ± 1.3	0.7 ± 0.3
1999ac	−18.84(96)	0.98(08)	0.57	32.99(96)	$d = cz/H_o$[f]	7	(0.046)	···	0.24(06)	0.098(030)	4.6	9.0 ± 3.4	6.0 ± 2.0
1999aw	−19.24(47)	0.75(10)	0.16[e]	35.99(47)	$d = cz/H_o$[f]	8	0.032(0.2)	4	0.07(06)	−0.024(025)	16.4	-24.9 ± 2.7	1.0 ± 0.8
1999bp	−19.37(33)	0.70(06)	0.01[e]	37.53(33)	$d = cz/H_o$[f]	9	(0.034)	···	0.15(03)	0.081(011)	16.9	-1.9 ± 1.2	-1.6 ± 0.3
1999by	−17.15(23)	1.90(05)	0.96[e]	30.74(23)	Cepheids	10	0.03(02)	5	0.63(05)	0.485(018)	< 1[g]	(176.1 ± 4.7)[i]	···

[a] Uncertainties given between brackets, in units of 0.01 mag.
[b] Uncertainties given between brackets, in units of 0.01.
[c] Uncertainties given between brackets, in units of 0.001.
[d] Adopted uncertainty in t_{br}: 0.5d.
[e] Outside the range $0.85 < \Delta m_{15}(B) < 1.70$ given by Phillips et al. (1999).
[f] Adopted $H_o = 72 \pm 3$ km s^{-1} Mpc^{-1}.
[g] Upper limit corresponding to the earliest observed epoch.
[h] Measured on the spectrum at maximum light.
[i] Extrapolated from a measurement at day +1, using the slope found through the inverse of Eqn. 6.
[j] REFERENCES: (1) Freedman et al. (2001); (2) Phillips (1993); (3) Gibson & Stetson (2001); (4) Turatto et al. (1996); (5) Della Valle et al. (1998); (6) Drenkhahn & Richtler (1999); (7) Jha (2002); (8) Strolger et al. (2002); (9) Reignault (2000); (10) Garnavich et al. (2001).
[k] REFERENCES: (1) Phillips et al. (1999); (2) Turatto et al. (1996); (3) Drenkhahn & Richtler (1999); (4) Strolger et al. (2002); (5) Garnavich et al. (2001).

tions from the estimates of the peak magnitudes and the distances.

5.1. Peak Luminosity

5.1.1. EW Ratios

The line depth ratio of the two absorptions troughs labeled as "Si II 5800" and "Si II 6150" on spectra around maximum light, $\mathcal{R}$(Si II), was introduced by Nugent et al. (1995) as a quantity which is correlated to luminosity. A similar spectral signature is introduced here: the EW ratio of "Si II 5800" to "Si II 6150", which we denote as $\mathcal{R}(\text{Si II})_{\text{EW}}$.

The EW ratio for each SN is computed at the time of maximum light by fitting a straight line to all the values of $\mathcal{R}(\text{Si II})_{\text{EW}}$ in the range $-7 <$ epoch $< +8$. For SNe with only one measurement off maximum light, this was extrapolated using the average slope of all other SNe —found to be 0.013 ± 0.004 d^{-1}. Uncertainties were propagated accordingly. Columns 7 and 8 of Table 8 respectively show $\mathcal{R}(\text{Si II})_{\text{EW}}$ and $\mathcal{R}$(Si II). The values of $\mathcal{R}$(Si II) for the SNe published in Nugent et al. (1995) were used. For the rest of the SNe in our sample, their method was reproduced for all spectra taken in the range $-7 <$ phase $< +8$ and the values at maximum light were derived, as described in the case of EW ratios. The analogy between the two kinds of Si II ratios is seen in Fig. 10, which shows their correlation with $M_B^{\max}$. A linear law reduces the dispersion in $M_B^{\max}$ for this sample of 13 SNe Ia from 0.89 mag to 0.33 mag for $\mathcal{R}$(Si II) and 0.39 mag for $\mathcal{R}(\text{Si II})_{\text{EW}}$.

There is a strong correlation between $\mathcal{R}$(Si II) and $\mathcal{R}(\text{Si II})_{\text{EW}}$. This would suggest that any possible change of the line profiles for different types of SNe Ia affects the two features in the same manner, making it equivalent to use either line depths or EW. Since when measuring an EW one uses the data from the whole absorption trough, instead of only the central part, we would expect $\mathcal{R}(\text{Si II})_{\text{EW}}$ to produce more robust results in the cases of spectra with low signal-to-noise ratios.

5.1.2. "Mg II 4300" Break

The evolutionary behavior of "Mg II 4300" is found to be correlated to photometric properties, as mentioned in Sec. 4.3. To quantify this correlation, the functional model given by Eqn. 3 was used to fit the parameter t_{br} for each of SN individually. This parameter is related to the phase in which this feature suddenly becomes stronger (what we call the "Mg II 4300" break). Column 9 of Table 8 lists the values of t_{br} for ten SNe Ia in our sample. In the cases of SN 1991bg and SN 1999by, the epochs of their earliest spectra are used as upper limits for t_{br}, assuming they followed the same evolutionary pattern found for the other objects.

The upper panel of Fig. 11 shows the correlation between $\Delta m_{15}(B)$ and t_{br}. The break occurs at later epochs for SNe with slower declining lightcurves. A least-squares fit with weights on both axes yields:

$$\Delta m_{15}(B) = 1.869(\pm 0.052) - 0.070(\pm 0.005) \cdot t_{br}, \quad (4)$$

where $1.7 < t_{br} < 16.9$ is given in days since maximum light. The fit was done excluding the two upper limits and the interesting case of SN 1999ac (see the coment on this SN in Sec. 2), which deviates by more than 5 standard deviations. The resulting dispersion in $\Delta m_{15}(B)$ around the fitted line is 0.08 mag, which is comparable with the measurement uncertainties.

The lower panel of Fig. 11 shows the correlation between $M_B^{\max}$ and t_{br}. A least-squares fit of a parabola yields:

$$M_B^{\max} = -17.29(\pm 0.52) - 0.30(\pm 0.11) \cdot t_{br} + \\ + 0.0102(\pm 0.0005) \cdot t_{br}^2. \quad (5)$$

The parabolic law was chosen in view of the relationship between $\Delta m_{15}(B)$ and $M_B^{\max}$ given by Phillips et al. (1999). The scatter in $M_B^{\max}$ for this sample is reduced from 0.49 to 0.21 mag. Note that this correlation includes the case of SN 1999ac which is deviating in $\Delta m_{15}(B)$.

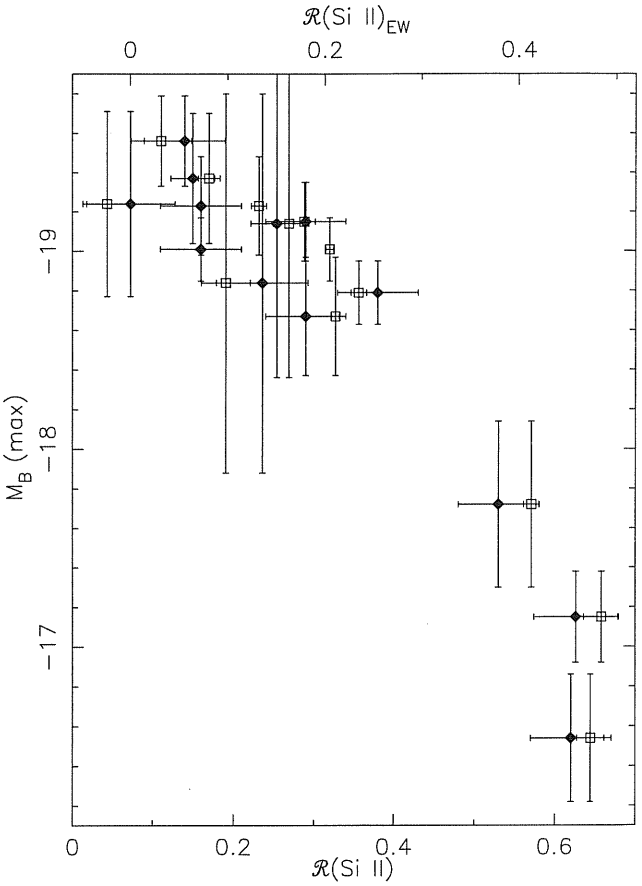

Fig. 10. Absolute magnitude at maximum light, $M_B^{\max}$, versus the silicon ratios, $\mathcal{R}$(Si II) as defined in Nugent et al. (1995) (*filled diamonds*), and $\mathcal{R}(\text{Si II})_{\text{EW}}$ (*open squares*).

Since this spectral feature lies almost exactly on the wavelength covered by the standard B filter, one would expect a correlation like the one found. An additional point to note is that this feature can be observed with optical detectors up to redshifts of ~1, which may make studies of this spectral region important for future SN-related cosmology experiments. Since several spectroscopic observations are needed to obtain the value of t_{br}, the use of this parameter to estimate $M_B^{\max}$ would be limited to SNe with rather extensive spectroscopic follow-up.

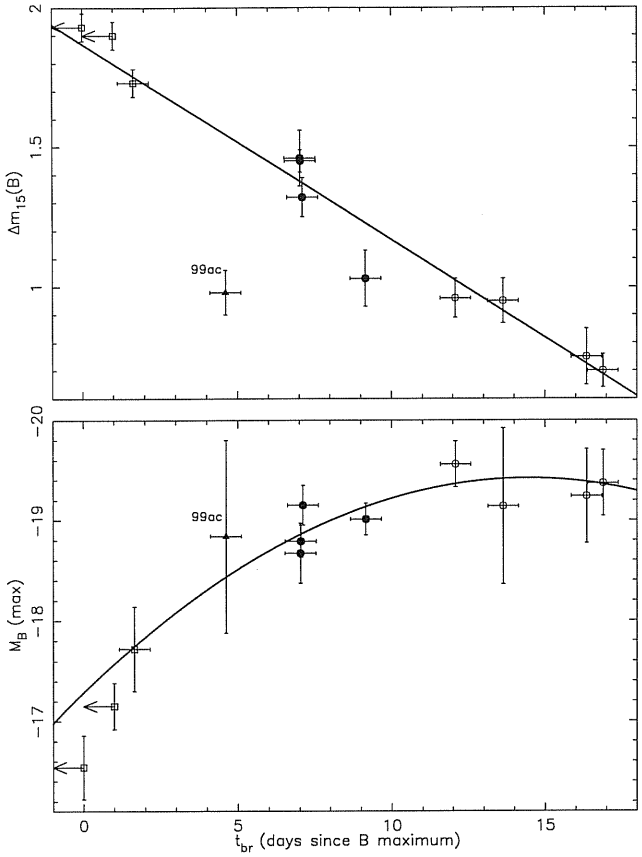

Fig. 11. The "Mg II 4300" break parameter t_{br}. *Upper panel*: $\Delta m_{15}(B)$ versus t_{br}. The two points marked with arrows correspond to upper limits of t_{br}. The straight line is least-squares fit to the data, excluding the upper limits and the oulying point corresponding to SN 1999ac. *Lower panel*: $M_B^{\max}$ versus t_{br} for the same objects as in the upper panel. The same two upper limits are marked with arrows. The solid line is a parabola fitted to the data, excluding the upper limits. SN 1999ac is included in the fit.

5.1.3. EW around Maximum Light

Some EW measurements around maximum light prove useful in finding correlations between spectral characteristics and absolute peak magnitudes. The strongest of such correlations comes from the behavior of the total absorption in the region from ~3900Å to ~4600Å, i.e. the sum of EW from features #2 and #3 ("Si II 4000" and "Mg II 4300"). These sums, which we name "$\mathrm{EW}_{(2+3)}$", were computed relative to an average value of 110Å, in the epoch range between −7 and +7 days. The time evolution of $\mathrm{EW}_{(2+3)}$ for single SNe in that epoch range can be described by a straight line. A least-squares method was used to fit the intercepts $[\mathrm{EW}^{\max}_{(2+3)}]$ and the slopes $[\alpha_{(2+3)}]$ of these lines for each SN. These values are listed in columns 10 and 11 of Table 8. They are found to correlate with $M_B^{\max}$. The strongest correlation is that of the $\alpha_{(2+3)}$ which is shown in the top panel of Figure 12. A least-squares fit of a straight line with weighs on both coordinates yields, for $-3.0 < \alpha_{(2+3)} < 13.2$ (Å d^{-1}):

$$M_B^{\max} = -19.27(\pm 0.10) + 0.103(\pm 0.025) \cdot \alpha_{(2+3)}. \quad (6)$$

The scatter in $M_B^{\max}$ for the present sample is reduced from 0.49 to 0.14 mag, a value which is below the typical uncertainties in $M_B^{\max}$. These uncertainties may be overestimated, especially due to the systematic uncertainties in the distances, which for the considered sample averages to $\sigma_{M_B} \sim 0.3$ mag. This correlation, if confirmed with larger data samples, would sharpen the normalization of $M_B^{\max}$ for SNe Ia and extend its applicability to $0.70 < \Delta m_{15}(B) < 1.73$.

Furthermore, we study the properties of $\alpha_{(2+3)}$ as a secondary calibrator of the standard candle, i.e. after $M_B^{\max}$ has been normalized using its correlation with $\Delta m_{15}(B)$. The bottom panel of Fig. 12 shows the residuals of that correlation (ΔM_B) against $\alpha_{(2+3)}$. A least-squares fit of a straight line yields:

$$\Delta M_B = -0.06(\pm 0.10) + 0.043(\pm 0.025) \cdot \alpha_{(2+3)}. \quad (7)$$

The dispersion in ΔM_B is reduced from 0.28 to 0.17 mag for the present sample. We note that the dispersion of 0.28 mag found after normalizing with $\Delta m_{15}(B)$ is larger than the one given by Phillips et al. (1999) because of the greater uncertainties in the magnitudes of the present sample and because several objects lie outside the range of $\Delta m_{15}(B)$ in which the normalization was defined by the authors. This correlation should be tested with larger data samples in order to determine if the combination of the two parameters proves more convenient than using a single parameter.

Similarly, $\alpha_{(2+3)}$ was combined as a secondary calibrator with the parameter t_{br} described in Sec. 5.1.2. However, for the SN sample considered in this work, this did not seem to reduce the scatter in the residuals of Eqn. 5. Evidently, a larger SN sample is needed to pursue this analysis.

The robustness of the estimates of $\alpha_{(2+3)}$ with respect to possible host-galaxy contamination was tested, especially since this spectral indicator might be useful to calibrate the brightness of supernovae at high-redshifts. Taking the case of a well-sampled SN, we artificially produced SN+host spectra by adding type E and Sc template galaxy spectra. These were added in amounts to simulate a range of contamination levels between 0 and 50% of the

total B-band flux, for the spectrum closer to maximum light. Under the conservative assumption that no further attempts are done to reduce the level of contamination when the SN is fainter, the rest of the SN spectra were scaled according to the B-band lightcurve measurements, thus increasing the effective amount of contamination introduced at those epochs. Figure 13 shows the results of this test. The upper panel shows the variation found on $\alpha_{(2+3)}$ as a function of contamination level. The lower panel shows the effect on absolute magnitudes, following the relation between $\alpha_{(2+3)}$ and $M_B^{\max}$ (Eqn. 6). It can be seen in this case, that the effect on the estimated luminosity is limited to less than ~ 0.1 mag for contamination levels as high as 50%.

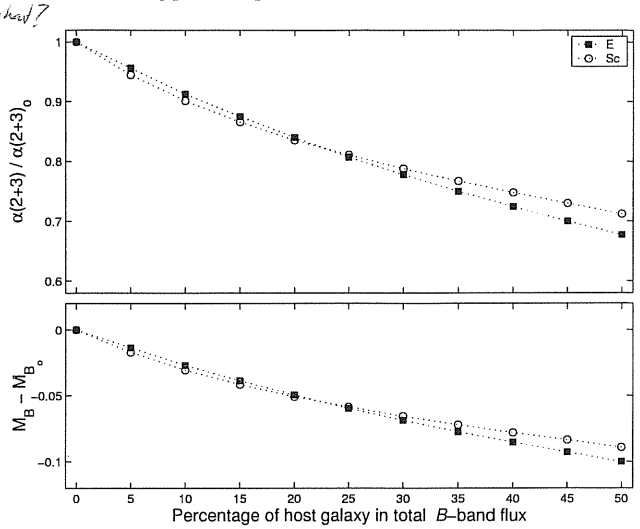

Fig. 13. The effect of host-galaxy contamination on $\alpha_{(2+3)}$ (*upper panel*) and on $M_B^{\max}$ (*lower panel*), through Eqn. 6. Filled squares correspond to a host galaxy of Hubble type E, while open circles correspond to one of type Sc. The values of the ordinates are given with respect to the non-contaminated case which is denoted with a zero subscript.

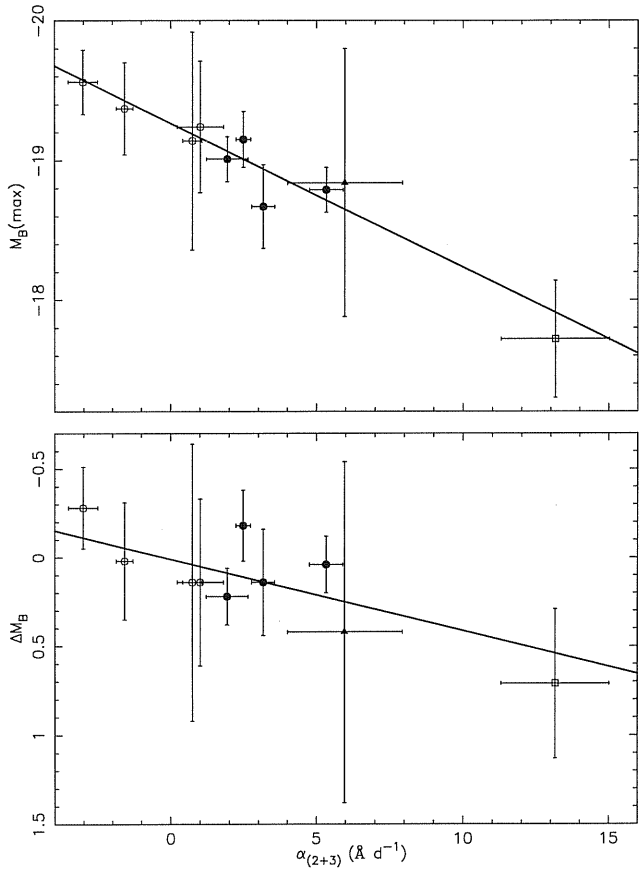

Fig. 12. The slope parameter $\alpha_{(2+3)}$. *Upper panel*: The correlation between $M_B^{\max}$ and $\alpha_{(2+3)}$ (see text). The solid line shows the fit of a straight line (Eqn. 6). *Lower panel*: Residuals (ΔM_B) of the correlation between $M_B^{\max}$ and $\Delta m_{15}(B)$ (Phillips et al., 1999) versus $\alpha_{(2+3)}$. The correlation between ΔM_B and $\alpha_{(2+3)}$ is represented by the straight line (Eqn. 6).

The computation of $\alpha_{(2+3)}$ can be done using a minimum of two spectra taken around maximum light. This and the location on the spectrum of the features involved makes it practicable on optical spectra of SNe up to $z \sim 1$. We tested its applicability on a SN at $z = 0.55$ observed on two epochs with an eight-metre class telescope and a total exposure time of ~4 hours. We were able to estimate $\mathrm{EW}_{(2+3)}^{\max}$ with an uncertainty of ~10Å, and $\alpha_{(2+3)}$ with an error of ~2.5Åd^{-1}. The latter would correspond, through Eqn. 6, to an uncertainty of ~0.25 in $M_B^{\max}$. The use of $\alpha_{(2+3)}$ could thus provide sufficiently precise luminosities in an independent manner of those coming from lightcurve measurements.

6. Conclusions

We have introduced a set of newly defined spectroscopic measurements for SNe Ia. Equivalent width measurements (EW) on eight separate spectral features were performed. These EW's were used as an empirical tool to investigate the standard candle properties of SNe Ia: their homogeneity, evolution with phase and means of calibrating their intrinsic luminosities.

A remarkable degree of homogeneity among SNe Ia was found, including both 1991T- and 1991bg-like objects, in the cases of features "Fe II 4800", "Mg II 4300" and "Ca II IR". Average evolutionary curves were built for Branch normal SNe to represent the general change of EW in time. The mean deviations of peculiar SNe were computed from those curves to help characterizing the different SNe Ia subtypes. We found that individual SNe evolve nearly parallel to each other. Also, we note a general trend of increasing EW from 1991T-like through normals and to 1991bg-like SNe.

The inhomogeneities among SNe Ia subtypes stand out in the cases of the Si II features ("Si II 4000", "Si II 5800" and "Si II 6150"). At times around maximum light the EW of these features serve to distinguish clearly among SNe Ia subtypes. The trend of increasing EW from 1991T-

like to 1991bg-like SNe is enhanced for "Si II 4000" and "Si II 5800". A more qualitative inhomogeneity was seen in the cases of "Ca II H&K" and "S II W", where large dispersions were found and evolutionary trends varied irrespective of the SN Ia subtype.

Several spectral parameters connected with the EW's were studied with emphasis on searching for possible correlations with intrinsic luminosity and lightcurve properties. Strongest correlations were found for $\mathcal{R}(\mathrm{Si\ II})_{\mathrm{EW}}$, t_{br}, and $\alpha_{(2+3)}$, defined in Sec. 5. The correlation of $\mathcal{R}(\mathrm{Si\ II})_{\mathrm{EW}}$ to $M_B^{\max}$ is similar to that found by Nugent et al. (1995) using line depth ratios. The parameter t_{br} reduces the scatter in $M_B^{\max}$ from 0.49 to 0.26 mag on a sample of ten SNe Ia in the range $0.70 < \Delta m_{15}(B) < 1.73$. Although the use of t_{br} is limited to SNe with rather extensive spectroscopic follow-up, the location of the measured feature on the blue part of the spectrum makes it applicable in principle to optical spectra of SNe up to $z \sim 1$.

Based on only ten SNe Ia, the correlation between $\alpha_{(2+3)}$ and $M_B^{\max}$ proved to reduce the scatter from 0.49 to 0.14 mag. We present this result as preliminary evidence that this parameter may sharpen the standard candle definition beyond the lightcurve shape-brightness relation. Clearly, these studies need to be confirmed with a larger statistical sample, e.g. from the SNfactory project (Aldering et al., 2002).

References

Aldering, G. et al. 2002, Proc. SPIE, 4836, 61
Barbon, R. et al. 1990, A&A, 237, 79
Branch, D. et al. 1983, ApJ, 270, 123
Branch, D., Drucker, W., & Jeffery, J. 1988, ApJ, 330, L117
Branch, D., Fisher, A., & Nugent, P. 1993, AJ, 106, 2383
Branch, D., & van den Bergh, S. 1993, AJ, 105, 2231
Cardelli, J. A., Clayton, G. C., & Mathis, J. S. 1989, ApJ, 345, 245
Cristiani, S. et al. 1992, A&A, 259, 63
Della Valle et al. 1998, MNRAS, 299, 267
Drenkhahn, G. & Richtler, T. 1999, A&A, 349, 877
Filippenko, A. V. et al. 1992, ApJ, 384, L15
Filippenko, A. V. et al. 1992, AJ, 104, 1543
Filippenko, A. V. 1997, ARA&A, 35, 309
Fisher, A. et al. 1999, MNRAS, 304, 67
Folatelli, G. et al. 2003 in prep.
Freedman, W. et al. 2001, ApJ, 553, 47
Gal-Yam, A. et al. 1999, IAU Circ. 7130
Garavini, G. et al. 2003 in prep.
Garnavich, P. M. et al. 2001, astro-ph/0105490
Gibson, B. K. & Stetson, P. B. 2001, ApJ, 547, L103
Goldhaber, G., Groom, D. E., Kim, A., et al. 2001, ApJ, 558, 359
Gray, D. F. 1992. *The observation and analysis of stellar photospheres*, Second Ed. Cambridge Univ. Press, p. 261
Hardin, D. et al. 2000, A&A, 362, 419
Hatano, K. et al. 2000, ApJ, 543, L49
Hillebrandt, W, & Niemeyer, J. C. 2000, ARA&A, 38, 191
Iben, I. Jr., & Tutukov, A. V. 1984, ApJS, 54, 335
Jeffery, D. et al. 1992, ApJ, 397, 304
Jha, S. 2002, PhD. Thesis, Harvard University
Kirshner, R. et al. 1973, ApJ, 185, 303
Kirshner, R. et al. 1993, ApJ, 415, 589
Knop, R. et al. 2003 (in prep.)
Leibundgut, B. et al. 1991, ApJ, 371, L23
Leibundgut, B. et al. 1993, AJ, 105, 301
Li, W. et al. 2001, PASP, 113, 1178
Li, W. et al. 2003, PASP, 115, 453
Lira, P. 1995, Masters Thesis, Univ. de Chile
Mazzali, P. A. et al. 1993, A&A, 269, 423
Mazzali, P. A. et al. 1995, A&A, 297, 509
Mazzali, P. A. et al. 1997, MNRAS, 284, 151
Meikle, W. P. S. et al. 1996, MNRAS, 281, 263
Nomoto, K. 1982, ApJ, 257, 780
Nugent, P. et al. 1995, ApJ, 455, L147
Paczyński, B., 1985 *Cataclysmic variables and low-mass X-ray binaries*, Dordrecht, D. Reidel Publishing Co., p. 1
Patat, F. et al 1996, MNRAS, 278, 111
Perlmutter, S. et al. 1997, AJ, 483, 565
Phillips, M. M. et al. 1987, PASP, 99, 592
Phillips, M. M. et al. 1992, AJ, 103, 1632
Phillips, M. M. 1993, ApJ, 413, L105
Phillips, M. M. et al. 1999, ApJ, 118, 1766
Phillips, M. M. et al. 2002, astro-ph/0211100
Reignault, N. 2000, PhD. Thesis, ...
Riess, A. et al. 1998, AJ, 116, 1009
Ruiz-Lapuente, P. et al. 1992, ApJ, 387, L33
Saha, A. et al. 1996, ApJ, 466, 55
Saha, A. et al. 1997, ApJ, 486, 1
Saha, A. et al. 1999, ApJ, 522, 802
Saha, A. et al. 2001, ApJ, 551, 973
Schaefer, B. E. et al. 1999, ApJ, 524, L103
Schlegel, D. J., Finkbeiner, D. P., & Davis, M. 1998, ApJ, 500, 525
Strolger, L.-G. et al. 2002, AJ, 124, 2905
Sullivan, M. et al. 2003, MNRAS, 340, 1057
Tonry, J. L. et al. 2003, ApJ, 594, 1
Turatto, M. et al. 1996, MNRAS, 283, 1
Vinkó, J. et al. 2001, AJ, 121, 3127
Wang, L. et al. 2003, astro-ph/0303397
Wells, L. A. et al. 1994, AJ, 108, 2233
Wheeler J. C.; Harkness, R. P. 1990 Rep. Prog. Phys., 53, 1467
Whelan, J., & Iben, I. Jr. 1973, ApJ, 186, 1007